# Complex fragment emission in the 200-MeV $^4$He+$^{nat}$Ag, $^{197}$Au reactions

J. Zhang,* K. Kwiatkowski, D. Bonser, M. Fatyga,† S. D. Coon,‡ K. Stith, V. E. Viola, L. W. Woo,§ and S. J. Yennello**
*Departments of Chemistry and Physics and IUCF, Indiana University, Bloomington, Indiana 47405*
(Received 28 April 1997)

Spectra, angular distributions, and cross sections have been measured for $Z=3-14$ fragments produced in 200-MeV $^4$He-induced reactions on $^{nat}$Ag and $^{197}$Au targets. In addition, isotopic yields were measured at forward angles. Two-component moving-source fits have been performed on the data to evaluate the relative contributions of nonequilibrium and equilibrium emission mechanisms. At forward angles, the complex fragment yields are dominated by nonequilibrium emission, with IMF energies extending from the emission barrier to momenta in excess of the incident beam. Backward of 90° the yields are nearly isotropic and exhibit spectra consistent with emission from an equilibrated composite nucleus. [S0556-2813(97)03010-0]

PACS number(s): 25.70.Mn, 25.55.−e, 25.70.Gh

## I. INTRODUCTION

Measurements of intermediate-mass-fragment spectra (IMF: $3\leqslant Z\lesssim 15$) yield important signatures of the reaction dynamics associated with the formation and decay of hot nuclei. At bombarding energies near the IMF emission barrier, conditional saddle points and the statistical properties of equilibrated nuclei have been studied [1,2]. In the Fermi-energy regime, IMF spectra reflect the growing importance of nonequilibrium events, which represent a very fast collective phenomenon [3–5]. As the projectile energy exceeds a GeV or so, multiple fragment emission becomes highly probable, providing evidence for nuclear expansion and spinodal decomposition [6,7], perhaps yielding insights into the nuclear equation of state [8–10].

While evaporative emission of complex fragments is relatively well described by statistical models [11,12] and multifragmentation has received much current attention [8–10], nonequilibrium IMF emission poses a significant theoretical challenge [13,14]. Besides the intrinsic physics interest in describing the formation of complex clusters from a light-ion projectile on a time scale comparable to the nuclear transit time, a knowledge of these processes is an important practical consideration in the interpretation of both low-energy reactions and multifragmentation phenomena. Since the emission time scale is a continuous one, it is essential to isolate those events driven by collision dynamics from those originating from more equilibrated systems. This is particularly important in the case of multifragmentation, where IMF's from both processes are necessarily admixed.

In the experiments described here, we have examined two systems in which both equilibrium and nonequilibrium IMF emission play important roles in the reaction dynamics. The choice of the 200-MeV $^4$He+$^{nat}$Ag, $^{197}$Au reactions was motivated by several factors. Most important, the use of a light-ion projectile eliminates the strong contribution from projectile fragmentation processes that accompany heavy ion beams at forward angles, where nonequilibrium emission is most prominent.

The bombarding energy of $E/A=50$ MeV is sufficiently high to provide comparable yields of equilibrium IMF's, but not so high that the nonequilibrium IMF component dominates the cross sections [3,4]. Further, due to the exponentially increasing nature of the excitation function for IMF production in this bombarding energy regime, there is a high probability that equilibrium emission will occur primarily from collisions in which there is nearly full linear-momentum-transfer from projectile to target. This has been verified in measurements using the fission-fission-IMF angular correlation technique [15,16].

Experimentally, the separation of equilibrium and nonequilibrium IMF events imposes several constraints. Relatively low detector energy thresholds are required to obtain complete fragment spectra up to $Z\sim 15$ at backward angles, especially for lighter targets. Complete angular distributions are essential in order to characterize the rapidly rising cross sections at forward angles and the degree of isotropy at backward angles. In addition, isotope-identified data at very forward angles provide information on the nonequilibrium processes; backward-angle isotope measurements on similar systems have been reported previously [17].

This paper emphasizes the experimental results and the conclusions derived from a two-component, moving-source fit to the data, using the transition-state formalism of Ref. [18] to parametrize equilibrium emission and an *ad hoc* Maxwellian function to describe the nonequilibrium component of the yield [4,5].

## II. EXPERIMENTAL PROCEDURES

The experiment was performed at the Indiana University Cyclotron Facility with a $^4$He beam of 200-MeV incident energy. Pulse-selected 1:2 beams with currents up to 50 nA were used to irradiate targets in the IUCF 162-cm-diam. scattering chamber. The beam diameter was approximately 2 mm. Self-supporting, high-purity ($>$99.999%) targets of

*Present address: Institute of Atomic Energy, Beijing, PRC.
†Present address: Computerized Medical Systems, St. Louis, MO 63131.
‡Present address: Department of Chemistry, Northern Iowa University, Cedar Falls, IA 50614-0423.
§Present address: Sabbagh Associates, Bloomington, IN.
**Present address: Department of Chemistry, Texas A&M University, College Station, TX.

 

$^{nat}$Ag and $^{197}$Au of aereal density 1.9 mg/cm$^2$ were bombarded. To minimize possible light-element contamination of the spectra, freshly prepared targets were used and the vacuum system involved cryopumping of both the scattering chamber and the adjacent section of beam line. Spectra from carbon and blank targets were also measured to monitor possible sources of contamination from carbon buildup on the targets or beam halo. The growth of light-element contributions to the spectra can be monitored sensitively on line from examination of the two-dimensional particle-identification contours. For light elements bombarded with intermediate-energy alpha particles, the energy spectra fall in a region well below the Coulomb-like peaks for emission from Ag and Au residues, and in addition, the $^7$Be/$^9$Be is much larger [19,20]. On the basis of this analysis, light-element target-contamination problems were found to be negligible. Target thicknesses were determined by weight and area, as well as energy-loss measurements with a $^{241}$Am alpha spectroscopy source.

Inclusive IMF spectra were measured at randomly selected angles between 11° and 170° with a pair of detector telescopes. At forward angles, measurements were performed with a multiple-element isotope-identification telescope consisting of an axial-field gas-ionization counter [21], 300-$\mu$m surface-barrier detector, a 5-mm Li-drifted silicon detector, and a 12.7-cm NaI scintillator. The second telescope arm was used for charge identification only and employed an axial gas-ionization counter, a 300-$\mu$m silicon detector and a 5-mm Si(Li) detector. The gas-ionization chambers used $CF_4$ gas at a pressure of 45 Torr. Particle-identification thresholds were approximately 0.5 MeV/fragment nucleon and excellent charge resolution was achieved for fragments up to $Z \cong 14$. For the isotope-identification telescope, a Spieler [22] fast-timing pickoff was incorporated in the signal electronics. In conjunction with the cyclotron rf signal, this system provided fragment time-of-flight mass identification with a time resolution of about 250 ps, yielding discrete isotope resolution for fragments with $Z \leqslant 8$ and $A \leqslant 19$.

All detectors were calibrated with $^{241}$Am and $^{148}$Gd alpha spectroscopy sources and a precision pulse generator. The gas-ionization chamber procedure involved the measurement of energy-loss signals at several $CF_4$ gas pressures, along with corresponding alpha energy in the first silicon element. Corrections for fragment energy losses in the target (50% of the target thickness) and ion-chamber window were based on measured thicknesses and energy-loss tables [23].

Data acquisition was performed with the XSYS [24] system. Because of the low IMF cross sections and the very high counting rate of light-charged particles relative to IMF's, the Si(Li)/NaI detectors were operated in the veto mode for light-charged particles to minimize dead time.

### III. EXPERIMENTAL RESULTS

In Figs. 1 and 2, kinetic-energy spectra at representative laboratory angles are shown for boron fragments from the $^4$He+$^{nat}$Ag system and carbon fragments from the $^4$He+$^{197}$Au system, respectively. The spectra exhibit the Maxwellian shapes previously reported for similar systems, characterized by a Coulomb-like peak and an exponentially

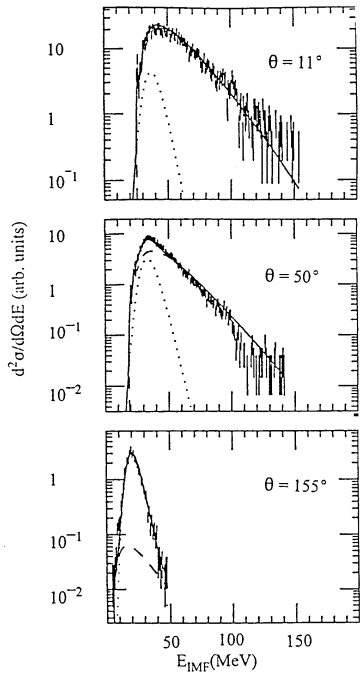


FIG. 1. Kinetic-energy spectra of boron fragments as a function of angle for the 200-MeV $^4$He+$^{nat}$Ag reaction.

falling tail that becomes increasingly steep in slope as the observation angle increases. This behavior is characteristic of all $Z \geqslant 5$ fragments and little dependence on isospin for a given element is observed. An important aspect of these measurements is that the Coulomb-like peak is clearly defined at the backwardmost angles for all $Z \leqslant 12$ fragments; this has an important influence on the results of the fitting procedures described in the following section. For Li and Be fragments, the high-energy tails of the spectra are more pro-

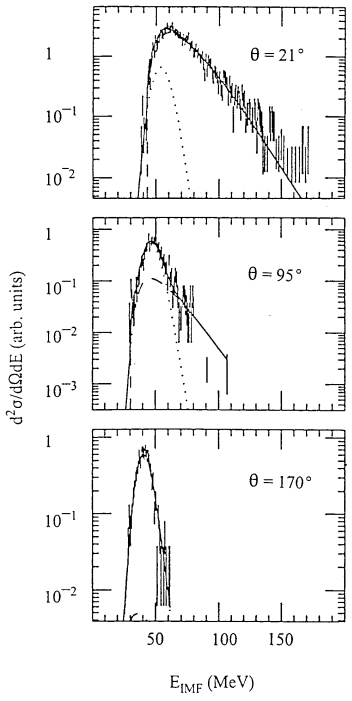


FIG. 2. Kinetic-energy spectra of carbon fragments as a function of angle for the 200-MeV $^4$He+$^{197}$Au reaction.

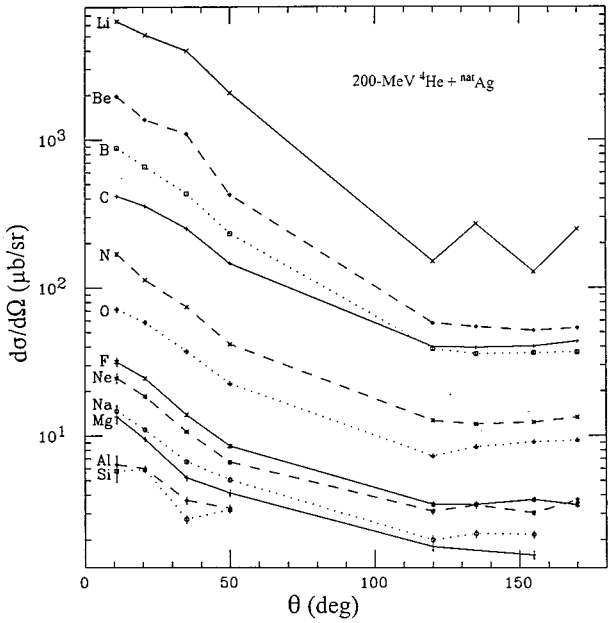


FIG. 3. Angular distributions of $Z=3-14$ fragments for the 200-MeV $^4$He+$^{nat}$Ag reaction.

nounced, with the $^7$Be/$^9$Be isotope ratio increasing strongly with IMF kinetic energy. This behavior has been discussed in previous publications [5,25,26].

Laboratory angular distributions for all fragments are shown in Figs. 3 and 4 for the $^{nat}$Ag and $^{197}$Au targets, respectively. Strong forward peaking of the differential cross sections is apparent for both targets, but is most pronounced for Ag. The forward-to-backward cross-section ratios evolve toward increasingly isotropic behavior as a function of IMF charge. However, for all fragments up to Na, these ratios significantly exceed expectations for statistical emission from a complete fusion source, transformed into the laboratory frame. This observation implies that a significant fraction of the IMF spectra observed at forward angles has a dynamic origin in which up to 10–20 nucleons are accreted on a time scale of the order of the nuclear transit time, acquiring momenta up to 50% greater than the beam momentum. In contrast, in the backward hemisphere the yields for all IMF's are essentially isotropic, which combined with corresponding spectral slopes implies emission from an equilibrated system. The most-probable IMF kinetic energies are also in good agreement with fission kinetic-energy systematics [27].

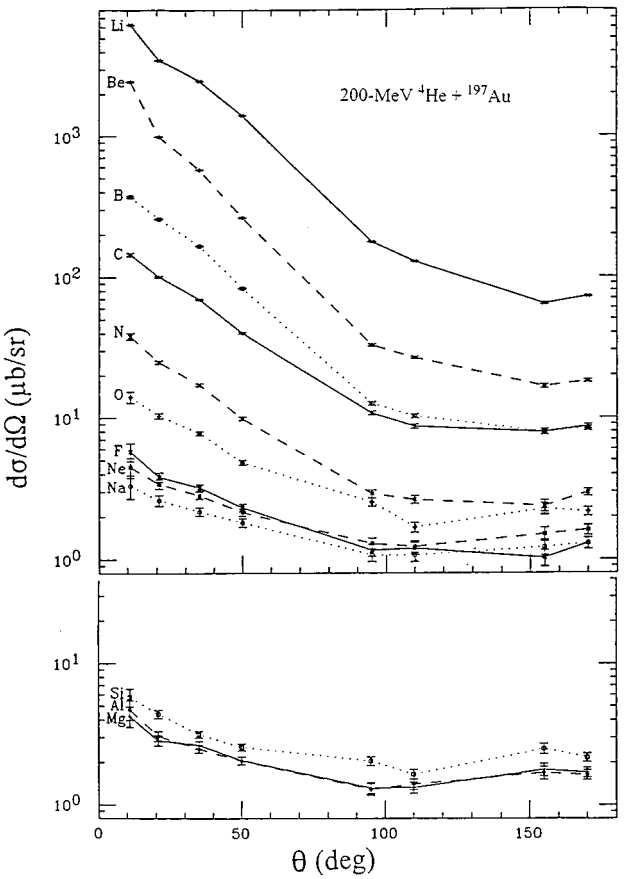


FIG. 4. Angular distributions of $Z=3-14$ fragments for the 200-MeV $^4$He+$^{197}$Au reaction.

TABLE I. Cross sections for the 200-MeV $^4$He+$^{nat}$Ag system.

| $Z$ (IMF) | $\sigma_{tot}$ ($\mu$b) | $\sigma_{EQ}$ ($\mu$b) | $\sigma_{NEQ}$ ($\mu$b) | $\sigma_{EQ}/\sigma_{tot}$ |
|---|---|---|---|---|
| 3 | $15\times10^3$ | $2.2\times10^3$ | $13\times10^3$ | 0.15 |
| 4 | $3.9\times10^3$ | 680 | $3.2\times10^3$ | 0.17 |
| 5 | $1.7\times10^3$ | 440 | $1.3\times10^3$ | 0.26 |
| 6 | $1.1\times10^3$ | 520 | 580 | 0.47 |
| 7 | 340 | 170 | 170 | 0.50 |
| 8 | 190 | 120 | 70 | 0.61 |
| 9 | 74 | 44 | 30 | 0.59 |
| 10 | 59 | 44 | 15 | 0.75 |
| 11 | 49 | 39 | 10 | $\geqslant$0.80 |
| 12 | 43 | 34 | 9 | $\geqslant$0.80 |
| Total | 22 mb | 4.3 mb | 18 mb | |

The total cross sections as a function of IMF charge are tabulated in Tables I and II for the $^{nat}$Ag and $^{197}$Au targets, respectively. These results yield total IMF cross sections of 22 mb for the $^4$He+$^{nat}$Ag system and 13 mb for $^4$He+$^{197}$Au. Thus, the IMF yields constitute only about 1% of the reac-

TABLE II. Cross sections for the 200-MeV $^4$He+$^{197}$Au system.

| $Z$ (IMF) | $\sigma_{tot}$ ($\mu$b) | $\sigma_{EQ}$ ($\mu$b) | $\sigma_{NEQ}$ ($\mu$b) | $\sigma_{EQ}/\sigma_{tot}$ |
|---|---|---|---|---|
| 3 | $9.8\times10^3$ | 880 | $8.9\times10^3$ | 0.09 |
| 4 | $2.0\times10^3$ | 240 | $1.8\times10^3$ | 0.12 |
| 5 | 600 | 78 | 520 | 0.13 |
| 6 | 290 | 100 | 190 | 0.34 |
| 7 | 74 | 33 | 41 | 0.44 |
| 8 | 39 | 25 | 15 | 0.63 |
| 9 | 19 | 14 | 5 | 0.72 |
| 10 | 19 | 16 | 3 | 0.85 |
| 11 | 18 | 16 | 2 | 0.88 |
| 12 | 23 | 20 | 2 | $\geqslant$0.90 |
| 13 | 23 | 20 | 2 | $\geqslant$0.90 |
| 14 | 30 | 27 | 2 | $\geqslant$0.90 |
| Total | 13 mb | 1.5 mb | 11 mb | |

TABLE III. Isotopic differential cross sections for the 200-MeV $^4$He+$^{nat}$Ag, $^{197}$Au reactions measured at a laboratory angle of 20°.

| Fragment | $d\sigma/d\Omega$ ($\mu$b/sr) | | Fragment | $d\sigma/d\Omega$ ($\mu$b/sr) | |
|---|---|---|---|---|---|
| | $^{nat}$Ag | $^{197}$Au | | $^{nat}$Ag | $^{197}$Au |
| $^6$Li | 1990 | 880 | $^{10}$C | 5.2 | 1.6 |
| $^7$Li | 2630 | 1730 | $^{11}$C | 34 | 8.4 |
| $^8$Li | 360 | 350 | $^{12}$C | 170 | 38 |
| $^9$Li | 59 | 110 | $^{13}$C | 110 | 37 |
| | | | $^{14}$C | 36 | 19 |
| $^7$Be | 650 | 220 | $^{15}$C | 4.3 | 2.8 |
| $^9$Be | 440 | 290 | | | |
| $^{10}$Be | 230 | 210 | $^{13}$N | 3.8 | 0.5 |
| | | | $^{14}$N | 32 | 5.5 |
| $^8$B | 10 | 2.6 | $^{15}$N | 55 | 13 |
| $^{10}$B | 230 | 66 | $^{16}$N | 7.6 | 2.8 |
| $^{11}$B | 360 | 150 | $^{17}$N | 3.7 | 2.1 |
| $^{12}$B | 44 | 31 | | | |
| $^{13}$B | 9.1 | 9.4 | $^{15}$O | 4.3 | 0.3 |
| | | | $^{16}$O | 25 | 2.8 |
| | | | $^{17}$O | 13 | 2.0 |
| | | | $^{18}$O | 9.0 | 2.5 |
| | | | $^{19}$O | 1.9 | 0.9 |

tion cross section: $\sigma_R = 1830$ mb for the $^{nat}$Ag target and $\sigma_R = 2550$ mb for $^{197}$Au [28]. The lower IMF yield for the $^{197}$Au target is consistent with the higher Coulomb barrier for the higher $Z$ target. In Table III, the isotopic cross sections are listed for Li-O isotopes measured at 20° for both systems. A general feature of these isotopic yields is that the more neutron-excess target, $^{197}$Au ($N/Z = 1.49$), produces a higher fraction of neutron-excess IMF's relative to the $^{nat}$Ag target ($N/Z = 1.30$). This is shown for carbon isotopes in Fig. 5, a result that has been previously studied in more detail for the $^{116,124}$Sn+$^4$He systems [17]. It is interesting to note that the forward-angle isotopic distributions for 200-MeV $^4$He+$^{116}$Sn ($N/Z = 1.32$) are nearly identical to those observed here for $^{nat}$Ag. Those for $^{124}$Sn ($N/Z = 1.48$) strongly resemble the $^{197}$Au results. This correspondence implies a coalescencelike production mechanism for these largely nonequilibrium ejectiles that reflects the $N/Z$ ratio of the colliding species.

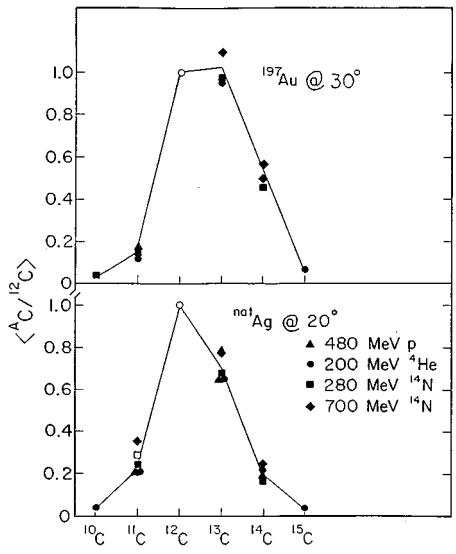


FIG. 5. Forward-angle isotope-yield ratios relative to $^{12}$C for $^{nat}$Ag (lower frame) and $^{197}$Au (upper frame) bombarded by various projectiles at several incident energies, as indicated in the figure. For $^{14}$N data, the projectile-fragmentation yield has been eliminated from the analysis.

Also shown in Fig. 5 are the forward-angle isotope ratios for carbon fragments emitted from $^{nat}$Ag and $^{197}$Au bombarded by a variety of projectiles over a broad range of bombarding energies. The striking independence of these ratios on projectile type and bombarding energy is also valid for other $Z$ fragments in Table III. In fact, comparison of these results with 300 GeV $p$+Xe data [29] yields a comparable pattern. For example, if one takes ratios of adjacent isotopes $(Z,N;Z,N+1)$ from Table III and compares with the data of Ref. [29], a value of $0.61 \pm 0.18$ is obtained for $^{nat}$Ag and $0.96 \pm 0.21$ for $^{197}$Au for the 21 adjacent pairs of isotopes in Table III.

Double-isotope ratios have recently been employed as a thermometer for measuring the temperature of hot nuclear matter [30–32]. The observed independence of these ratios on collision conditions suggests that either (1) the freezeout conditions for these (largely) nonequilibrium fragments are nearly independent of the reaction dynamics, or (2) the isotopic thermometer may not be a reliable method of determining nuclear temperatures. For the present data we have calculated average temperatures from the data in Table III for which the isotope binding-energy difference is $B > 10$ MeV, corrected according to the systematics of Ref. [32]. Compound-nucleus formation and a level-density parameter of $a = A/8$ MeV$^{-1}$ predicts a maximum temperature of 3.6 MeV for the $^{nat}$Ag system and 2.7 MeV for $^{197}$Au.

Despite the clearly nonequilibrium nature of the spectra at 20° in Figs. 1 and 2, the isotope-ratio temperature for the $^{nat}$Ag target is $T = 3.4$ MeV consistent with the compound nucleus prediction. In contrast, analysis [33] of the similar $^4$He+$^{116}$Sn system at backward angles [17] yields an isotope-ratio temperature $T = 2.7$ MeV, which would imply a relatively low average linear momentum transfer for collisions that produce IMF's from equilibrated systems. For the $^{197}$Au target, the isotope-ratio temperature at 20° is $T = 3.6$ MeV, well above both the compound nucleus value and an isotope thermometer value of $T = 2.8$ MeV determined from backward-angle data for the comparable $N/Z$ $^4$He+$^{124}$Sn system. It is also of interest to note that the isotope-ratio temperatures for $^{nat}$Ag and $^{197}$Au at 20° are nearly the same as that for the 300 GeV $p$+Xe reaction [29] taken at 48°, $T = 3.9$ MeV. These temperature results are analyzed in a broader context in Ref. [33].

## IV. MOVING-SOURCE FITS

In order to evaluate the relative contributions of equilibrium (EQ) and nonequilibrium (NEQ) mechanisms to the IMF yields, a simultaneous two-component moving-source fit has been performed on these data. The fitting procedure is discussed in detail in Refs. [5,16]. While this is schematic in nature, the strong differences between the forward-hemisphere and backward-hemisphere results suggest that

TABLE IV. Moving-source fit parameters for the 200-MeV $^{4}$He+$^{nat}$Ag system.

| | $Z_{IMF}$ | 5 | 6 | 7 | 8 | 9 | 10 |
|---|---|---|---|---|---|---|---|
| EQ | $\beta_{EQ}$ | 0.0117 | 0.0117 | 0.0117 | 0.0117 | 0.0117 | 0.0117 |
| | $T_{EQ}$ | 3.7 MeV | 3.7 MeV | 3.7 MeV | 3.7 MeV | 3.7 MeV | 3.7 MeV |
| | $k_{EQ}$ | 0.831 | 0.805 | 0.793 | 0.771 | 0.773 | 0.757 |
| | $p_{EQ}$ | 7.1 | 9.5 | 12.7 | 15.1 | 21.1 | 18.0 |
| | $\alpha$ | 0.7 | 0.7 | 0.7 | 0.7 | 0.7 | 0.7 |
| | Norm EQ | 9.45 | 12.9 | 5.12 | 4.22 | 2.46 | 2.04 |
| NEQ | $\beta_{NEQ}$ | 0.0247 | 0.0191 | 0.0182 | 0.0151 | 0.0130 | 0.0120 |
| | $T_{NEQ}$ | 13.0 MeV | 13.0 MeV | 13.0 MeV | 13.0 MeV | 13.0 MeV | 13.0 MeV |
| | $k_{NEQ}$ | 0.5 | 0.5 | 0.5 | 0.5 | 0.5 | 0.5 |
| | SIGCB | 3.0 | 3.0 | 3.0 | 3.0 | 3.0 | 3.0 |
| | $\theta$ | 30° | 30° | 30° | 30° | 30° | 30° |
| | Norm NEQ | $8.47\times10^{3}$ | $4.14\times10^{3}$ | $1.18\times10^{3}$ | 564 | 257 | 136 |
| | $x^2/N$ | 1.9 | 2.4 | 1.8 | 1.6 | 1.2 | 1.6 |

the approximations below have at least empirical validity.

The equilibrium source was assumed to be the binary decay of an equilibrated targetlike residue. The spectral shapes were parametrized in terms of the scission-point model of Moretto [18], which includes a mean source velocity $v_{EQ}$; temperature $T_{EQ}$; fractional Coulomb barrier $k_{EQ}$; a $Z$-dependent amplification parameter $p$, that permits evolution of the fragment shapes with IMF charge; and an anisotropy parameter $\alpha$, to account for possible forward-backward peaking of the symmetric angular distributions, where $w(\theta)\alpha(1+\alpha\cos^4\theta)$ in the source frame.

Whereas statistical models are generally successful in describing equilibrium processes, the understanding of nonequilibrium emission is complicated by the short time scales and close coupling between the collision dynamics and the final state. Consequently, we employ a phenomenological approach and approximate the small-angle spectra (shown in Figs. 1 and 2) with a Maxwellian-like function with surface emission. The parameters of this component include a fast-source velocity $v_{NEQ}$; slope temperature $T_{NEQ}$; fractional Coulomb barrier and spreading width $k_{NEQ}$; and SIGCB, and an empirical angular distribution function, $w(\theta)\alpha\exp(-\theta)$ in the source frame of reference.

The parameters of both EQ and NEQ components, along with their respective normalization factors and chi-squared per degree of freedom values, are tabulated for $Z=5-10$ fragments in Tables IV and V. Values for $Z=3$ and 4 were not included in the fits, since these components are strongly dominated by nonequilibrium emission. The quality of the fits to the spectra is indicated in Figs. 1 and 2, where the equilibrium component is given by the dotted lines, the nonequilibrium component by the dot-dashed lines, and the sum by solid lines. One qualitative observation of these fits is that the nonequilibrium component at forward angles contains a significant fraction of events with energies near the Coulomb-like peak of the equilibrium component. Thus, these low-energy fragments, that appear to be formed via accretionlike processes [34,35] on a fast-to-intermediate time scale, are indistinguishable from fragments originating from fully equilibrated events.

The fitting parameters for the equilibrium source are consistent with emission from an equilibrated compound nucleus. For consistency, in the final fits the same average source velocity and temperature parameters were applied to all $Z=5-10$ IMF's. The fit values of $v_{EQ}=0.012c$ and $T_{EQ}=3.7$ MeV for the $^{nat}$Ag target are in good agreement with

TABLE V. Moving-source fit parameters for the 200-MeV $^{4}$He+$^{197}$Au system.

| | $Z_{IMF}$ | 5 | 6 | 7 | 8 | 9 | 10 |
|---|---|---|---|---|---|---|---|
| EQ | $\beta_{EQ}=v_{EQ}/c$ | 0.00652 | 0.00652 | 0.00652 | 0.00652 | 0.00652 | 0.00652 |
| | $T_{EQ}$ | 2.8 MeV | 2.8 MeV | 2.8 MeV | 2.8 MeV | 2.8 MeV | 2.8 MeV |
| | $k_{EQ}$ | 0.860 | 0.828 | 0.818 | 0.780 | 0.794 | 0.767 |
| | $p_{EQ}$ | 8.8 | 17.8 | 31.4 | 34.2 | 34.3 | 41.6 |
| | $\alpha$ | 0.333 | 0.333 | 0.333 | 0.333 | 0.333 | 0.333 |
| | Norm EQ | 4.28 | 12.0 | 13.6 | 13.3 | 7.56 | 16.9 |
| NEQ | $\beta_{NEQ}$ | 0.0179 | 0.0130 | 0.0109 | 0.0098 | 0.0074 | 0.0070 |
| | $T_{NEQ}$ | 12.0 MeV | 12.0 MeV | 12.0 MeV | 12.0 MeV | 12.0 MeV | 12.0 MeV |
| | $k_{NEQ}$ | 0.70 | 0.70 | 0.70 | 0.70 | 0.70 | 0.70 |
| | SIGCB | 3.0 | 3.0 | 3.0 | 3.0 | 3.0 | 3.0 |
| | $\theta$ | 25° | 25° | 25° | 25° | 25° | 25° |
| | Norm NEQ | $5.04\times10^{3}$ | $1.98\times10^{3}$ | 441 | 159 | 58.9 | 33.6 |
| | $x^2/N$ | 2.0 | 1.6 | 1.2 | 0.9 | 0.9 | 0.8 |

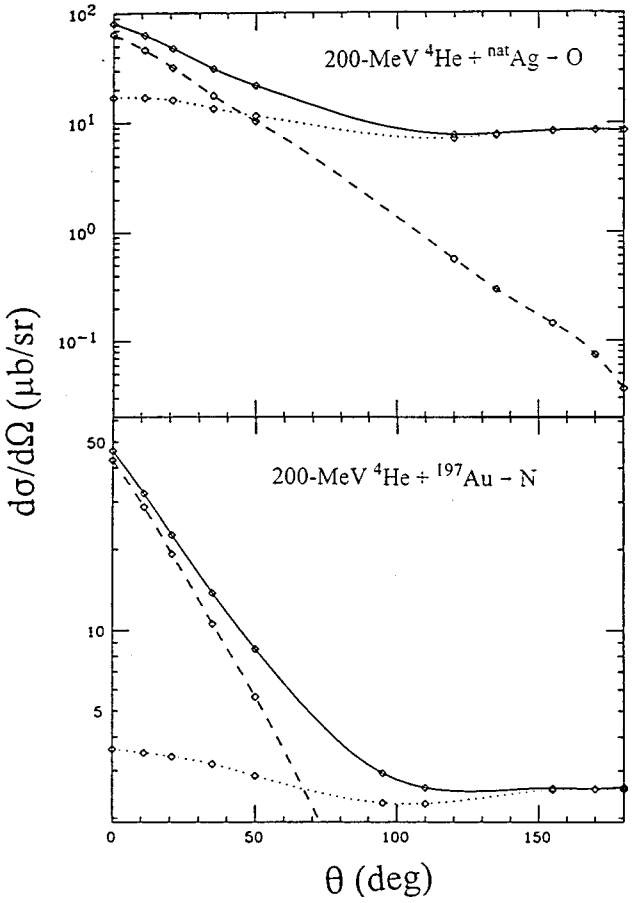


FIG. 6. Moving-source fits to the IMF spectra for equilibrium (dotted line), nonequilibrium (dashed line), and total (solid line). The upper frame is for oxygen fragments from the $^{nat}$Ag target and the lower frame is for nitrogen fragments from the $^{197}$Au target.

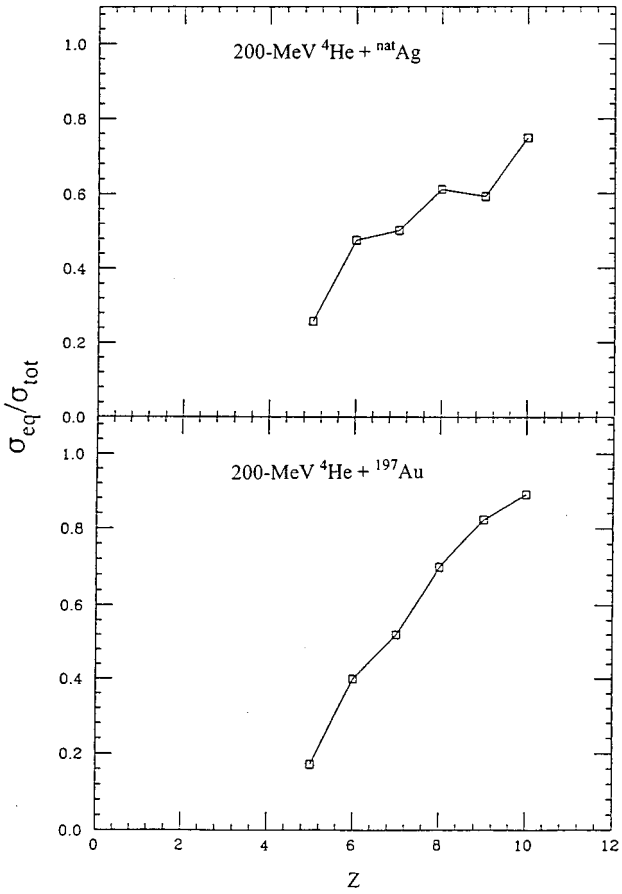


FIG. 7. Ratio of equilibrium-to-total IMF yields determined from moving source fits to $^{nat}$Ag spectra (upper frame) and $^{197}$Au spectra (lower frame).

values of $v_{EQ}=0.011c$ and $T=3.6$ MeV calculated for complete fusion and a level density parameter of $a=A/8$ MeV$^{-1}$. For the $^{197}$Au target, the moving-source fit gives values of $v_{EQ}=0.065c$ and $T_{EQ}=2.8$ MeV, to be compared with calculated values of $v_{EQ}=0.063c$ and $T_{EQ}=2.7$ MeV for the compound nucleus. The fractional Coulomb barrier parameters are about 80% that of touching spheres with $r_0=1.225A^{1/3}+2.0$ fm [1] and agree well with fission systematics [27]. The amplification-shape parameter $p$ increases systematically for both systems, reflecting the increased shape-barrier fluctuations with increasing fragment charge. The anisotropy parameter $\alpha$ is nonzero, but relatively small for both systems. For the equilibrium component this implies relatively small angular momenta for the emitting source, unlike $^{14}$N-induced reactions at these beam $E/A$ values, where significant backward peaking is observed [5].

The primary features of the nonequilibrium parameters are (1) source velocities two to three times greater than for the equilibrium source for lighter IMF's which systematically decrease toward the $v_{EQ}$ value with increasing IMF charge; (2) slope temperatures of 12–13 MeV, well in excess of those deduced for the equilibrium source; and (3) reduced fractional Coulomb barriers. These results are in general accord with other inclusive studies of IMF emission for which full energy spectra and angular distributions have been measured [3–5,17,24,26,36].

The relative contributions of the equilibrium and nonequilibrium sources are illustrated in Fig. 6, where the laboratory angular distributions for nitrogen fragments from the $^{nat}$Ag target and oxygen fragments from $^{197}$Au are plotted for the total fit (solid line), the equilibrium component (dotted line), and nonequilibrium component (dot-dashed line). The dominance of the nonequilibrium source at the most forward-angles and the equilibrium source at the most backward angles is apparent. In Table I, the total IMF cross sections for equilibrium emission, $\sigma_{EQ}(Z)$, for nonequilibrium emission, $\sigma_{NEQ}(Z)$, and the ratio $\sigma_{EQ}(Z)/\sigma_{tot}(Z)$ are tabulated. The ratio $\sigma_{EQ}(Z)/\sigma_{tot}(Z)$ is also plotted in Fig. 7 for both targets. The fraction of equilibrium events increases systematically from $Z=5$ to $Z=10$, illustrating that (1) nonequilibrium emission favors low-$Z$ fragments and (2) equilibrium emission (or very asymmetric fission) becomes increasingly important for higher-$Z$ fragments. This evolution is observed to be stronger for the $^{197}$Au target than for $^{nat}$Ag.

The success of this schematic two-component model in describing the evolution of the energy spectra and the angular distributions indicates that it provides a consistent qualitative picture of the physics that govern collisions near the Fermi energy. However, it must be stressed that any quantitative attempt to describe the dynamics of these processes must take into account the full time evolution of the system—which must necessarily involve a continuum of IMF emission stages.

TABLE VI. Charge distribution power-law exponents.

| | 200-MeV $^4$He+$^{nat}$Ag | 200-MeV $^4$He+$^{197}$Au |
|---|---|---|
| $\tau$ (total) | $4.7\pm0.2$ | $5.6\pm0.4$ |
| $\tau$ (EQ) | $3.2\pm0.2$ | $3.6\pm0.3$ |
| $\tau$ (NEQ) | $5.7\pm0.3$ | $6.5\pm0.4$ |

Finally, we have performed a power-law fit $\sigma(Z)\alpha Z^{-\tau}$ to the charge-distribution results in Tables I and II. The power-law exponents $\tau$ are summarized in Table VI. The charge distributions yield power-law exponents of $\tau=4.7\pm0.2$ for $^{nat}$Ag and $\tau=5.6\pm0.4$ for $^{197}$Au. The more rapid decrease in the cross sections as a function of IMF charge for $^{197}$Au is understood in terms of the greater Coulomb hindrance to charged-particle emission for the higher $Z$ system. For both nonequilibrium and equilibrium components, the power-law exponents are similar to those obtained in other light-ion studies [3,25], but are considerably larger than observed for the $^{14}$N+$^{nat}$Ag, $^{197}$Au systems [5]. As has been observed previously, the IMF charge distribution for nonequilibrium processes decreases with $Z_{IMF}$ much more rapidly than for the equilibrium component.

## V. CONCLUSIONS

In summary, we have investigated IMF emission in the 200-MeV $^4$He+$^{nat}$Ag, $^{197}$Au reactions. The data suggest that at least two major mechanisms are responsible for IMF formation: (1) a fast nonequilibrium process that produces fragments via an accretionlike mechanism with energies extending from the emission barrier up to values in excess of the beam momentum, well beyond those expectations for an equilibrated compound nucleus, and (2) statistical decay of an equilibrated heavy residue. A two-component, moving-source fitting procedure based on these assumptions provides a good description of the data. The equilibrium component exhibits properties expected for emission from an equilibrated nucleus produced in (near) complete fusion of the target and projectile, whereas the nonequilibrium component appears to originate from a much hotter source moving with a velocity significantly larger than the compound nucleus. The fit results also illustrate the strong dependence of the emission mechanism on IMF charge and angle, the nonequilibrium yield being dominated by low-$Z$ fragments at forward angles and the equilibrium yield being clearly separated at extreme backward angles.

Isotope ratios obtained at forward angles have also been measured. These are remarkably similar to ratios obtained from a wide variety of systems obtained at intermediate-to-high energies. Double isotope-ratio temperatures derived from these data are nearly identical to those obtained from $p+A$ reactions up to 300 GeV and the $^{14}$N+$^{nat}$Ag, $^{197}$Au reactions from $E/A=20-100$ MeV. This result suggests that either a limiting temperature near $T\approx4$ MeV describes all these systems or that the technique has low sensitivity to the temperature of the hot source.

The authors wish to express their thanks to Lee Sobotka and Warren Wilson for their contributions to this work. We also acknowledge the important contributions of Tim Ellison in tuning the IUCF rf phase-lock system, Dick Yoder for help with the data-acquisition program, Bill Lozowski for preparing the high-purity targets, and the operating staff at IUCF for providing excellent beams. This work was supported by the U.S. Department of Energy and the National Science Foundation.

[1] L. G. Sobotka *et al.*, Phys. Rev. Lett. **51**, 2187 (1983).
[2] M. A. McMahon, L. G. Moretto, M. L. Padgett, G. J. Wozniak, L. G. Sobotka, and M. G. Mustafa, Phys. Rev. Lett. **54**, 1995 (1985).
[3] R. E. L. Green and R. G. Korteling, Phys. Rev. C **22**, 1594 (1980).
[4] K. Kwiatkowski, J. Bashkin, H. Karwowski, M. Fatyga, and V. E. Viola, Phys. Lett. B **171**, 41 (1986).
[5] J. L. Wile *et al.*, Phys. Rev. C **45**, 2300 (1992).
[6] S. J. Yennello *et al.*, Phys. Rev. C **48**, 1092 (1993); K. Kwiatkowski *et al.*, Phys. Rev. Lett. **74**, 3756 (1995).
[7] R. T. deSouza *et al.*, Phys. Lett. B **300**, 29 (1993).
[8] J. Bondorf, R. Donangelo, I. N. Mishustin, C. J. Pethick, H. Schulz, and K. Sneppen, Nucl. Phys. **A443**, 321 (1985).
[9] W. A. Friedman, Phys. Rev. C **42**, 667 (1990).
[10] D. Gross, Rep. Prog. Phys. **53**, 605 (1990).
[11] R. Charity *et al.*, Nucl. Phys. **A483**, 371 (1988); computer code GEMINI, anon. FTP from WUNMR.WUSTL.EDU
[12] J. Gomez del Campo, Phys. Rev. Lett. **61**, 290 (1988).
[13] I. Cervasato *et al.*, Phys. Rev. C **45**, 2369 (1992); M. Cavinato *et al.*, Z. Phys. A **347**, 237 (1994).
[14] M. Blann, Phys. Rev. C **59**, 1341 (1996).
[15] M. Fatyga *et al.*, Phys. Rev. Lett. **58**, 2527 (1987); M. Fatyga *et al.*, Phys. Lett. B **185**, 321 (1987).
[16] D. E. Fields, Ph.D. thesis, Indiana University, 1992.
[17] J. Brzychczyk *et al.*, Phys. Rev. C **47**, 1553 (1993).
[18] L. G. Moretto, Nucl. Phys. **A247**, 211 (1975).
[19] A. Gokmen, H. Breuer, A. C. Mignerey, B. G. Glagola, K. Kwiatkowski, and V. E. Viola, Phys. Rev. C **29**, 1595 (1984).
[20] L. W. Woo, K. Kwiatkowski, W. G. Wilson, V. E. Viola, H. Breuer, and G. J. Mathews, Phys. Rev. C **47**, 267 (1993).
[21] K. Kwiatkowski, K. Komisarcik, J. L. Wile, S. J. Yennello, D. E. Fields, and V. E. Viola, Nucl. Instrum. Methods Phys. Res. A **299**, 166 (1990).
[22] H. Spieler, IEEE Trans. Nucl. Sci. **NS-29**, 1142 (1987).
[23] L. C. Northcliffe and R. F. Schilling, Nucl. Data, Sect. A **7**, 233 (1970).
[24] N. R. Yoder, IUCF Internal Report 85-4, 1985.
[25] E. Renshaw *et al.*, Phys. Rev. C **44**, 2618 (1991).
[26] R. E. L. Green, R. G. Korteling, and K. P. Jackson, Phys. Rev. C **29**, 1806 (1984).
[27] V. E. Viola, K. Kwiatkowski, and M. Walker, Phys. Rev. C **31**, 706 (1985).
[28] S. Kox *et al.*, Nucl. Phys. **A420**, 162 (1984).
[29] J. E. Finn *et al.*, Phys. Rev. Lett. **49**, 1321 (1982).

[30] S. Albergo, S. Costa, E. Costanzo, and A. Rubino, Nuovo Cimento A **89**, 1 (1985).
[31] J. Pochodzalla *et al.*, Phys. Rev. Lett. **75**, 1040 (1995).
[32] M. B. Tsang *et al.*, Phys. Rev. C **54**, R1057 (1996).
[33] V. E. Viola and K. Kwiatkowski, Indiana Report INC-116, 1997.
[34] D. H. Boal and R. M. Woloslyn, Phys. Rev. C **20**, 1878 (1979).
[35] W. G. Lynch and W. A. Friedman, Phys. Rev. C **28**, 16 (1983); **28**, 950 (1983).
[36] S. J. Yennello, K. Kwiatkowski, S. Rose, L. W. Woo, S. H. Zhou, and V. E. Viola, Phys. Rev. C **41**, 79 (1990).